Research Square

Preprints are preliminary reports that have not undergone peer review.
They should not be considered conclusive, used to inform clinical practice,
or referenced by the media as validated information.

Microstructure, Strength, Abrasive Wear and Cutting Forces of Vortex-Assisted Sand-Cast AA2014/SiC Composites: Effect of SiC Content

Berat Baris Buldum[1]
Mersin Üniversitesi
Recep Dabak[2]
İstanbul Gelişim Üniversitesi
Suleyman Cinar Cagan[1]
cinarcagan@mersin.edu.tr

Mersin Üniversitesi

Research Article

Keywords: AA2014 alloy, SiC reinforcement, sand casting, stir casting, abrasive wear, cutting force, strengthening mechanisms

Posted Date: November 23rd, 2026

DOI: https://doi.org/10.21203/rs.3.rs-11468669/v1

License: This work is licensed under a Creative Commons Attribution 4.0 International License.
Read Full License

Additional Declarations: No competing interests reported.

Abstract

Silicon carbide (SiC) is the most widely used particulate reinforcement for aluminum matrix composites, yet its effect on Al–Cu wrought alloys processed by low-cost sand casting is poorly documented. In this study, AA2014 matrix composites containing 3, 5 and 7 wt.% SiC were produced by vortex-assisted stir casting into sand molds. The composites were examined by optical and scanning electron microscopy and X-ray diffraction, and tested for Vickers hardness, ultimate tensile strength (UTS), two-body belt abrasion and cutting forces in dry turning. Particle-rich regions were located mainly in the interdendritic regions, and clustering with associated porosity became pronounced at 7 wt.%. XRD showed α-Al in all composites and resolved SiC clearly at 7 wt.%; neither Al_4C_3 nor free Si was detected, although a thin interfacial reaction layer cannot be excluded. Hardness rose monotonically from 33 HV for the unreinforced alloy to 64 HV at 7 wt.% SiC (+ 94%). UTS peaked at 143 MPa at 5 wt.% SiC (+ 55%) and fell to 121 MPa at 7 wt.%. Cumulative abrasive mass loss over 600 m decreased from 1.97 g to 1.49 g between 3 and 7 wt.% SiC, with a nearly constant Archard coefficient (0.022–0.024). Raising the SiC content from 3 to 7 wt.% increased the tangential and feed forces by 15–24%. A shear-lag estimate showed that load transfer accounts for less than 3 MPa of the strength gain, so matrix-side strengthening, most likely by thermal-mismatch dislocations and structural refinement, dominates. The 5 wt.% SiC composite offers the best balance of strength, wear resistance and machinability.

Introduction

Aluminum matrix composites (AMCs) reinforced with ceramic particles combine the low density and formability of aluminum alloys with the stiffness, hardness and wear resistance of a ceramic phase [1–3]. These properties have made them attractive for automotive, aerospace and defense components where monolithic alloys reach their limits [1, 3, 4]. Among the particulate reinforcements, SiC is used most widely, as it combines high hardness, a moderate density (≈ 3.2 g/cm³) and a low coefficient of thermal expansion (CTE) [1, 2]. SiC-reinforced aluminum is used in brake systems, pistons and thermal management parts [4, 5].

AA2014 is a heat-treatable Al–Cu–Mg–Si alloy used for aircraft fittings, truck frames and forged structural parts because of its high strength after precipitation hardening [6]. Like other 2xxx alloys, it has modest hardness and limited resistance to abrasive wear, which restricts its use in contact-loaded parts. Ceramic and nanoscale reinforcements have been shown to raise the hardness and strength of 2xxx alloys [7–9]. Reinforcing 2xxx alloys with SiC is therefore of practical interest. Recent work on 2014/SiC and 2024/SiC systems has addressed their processing and their mechanical and tribological behavior [10–12].

Liquid-state processing, and stir casting in particular, is the most economical route for producing particulate AMCs in large quantities and complex shapes [3, 13–15]. Three difficulties are well known, however. First, SiC is poorly wetted by molten aluminum, so particles tend to be rejected from the melt unless they are preheated or a wetting agent such as Mg is added [14, 16]. Second, the final particle

distribution depends on stirring speed, stirring time and stirrer geometry, and on settling and agglomeration during holding and pouring [1, 17–19]. During solidification, particles can also be pushed by the advancing solid–liquid interface and collect in the last liquid to freeze [20]. Third, SiC reacts with liquid aluminum through $4Al + 3SiC \rightarrow Al_4C_3 + 3Si$. The brittle carbide forms more readily at high melt temperatures and impairs ductility and toughness [16, 17]. A limited interfacial reaction may still improve bonding, whereas an extensive one degrades the composite [2, 16].

The effect of SiC content on cast AMCs has been studied extensively. Hardness and strength usually increase with SiC content [21–25]. Beyond a threshold, however, clustering and porosity reduce the strength and ductility [3, 10, 14, 26]. In sliding and abrasive wear, SiC particles reduce material loss by carrying part of the load and resisting micro-cutting, provided they remain bonded to the matrix [27–30]. At the same time, the hard SiC phase makes the composites difficult to machine: it raises cutting forces and accelerates abrasive tool wear [31–34]. Most of these studies concern Al–Si casting alloys, 6xxx and 7xxx alloys or powder-processed materials. They rarely report microstructure, strength, abrasion and cutting forces for the same set of samples.

The vortex-assisted sand-casting route used here was established in our earlier work on TiC-reinforced AA2014 [6], and TiC additions to AA2014 have also been examined by other groups [35]. For SiC, which is lighter and less expensive than TiC, the available AA2014 studies combine stirring with squeeze or ultrasonic treatment or with subsequent friction stir processing [10, 11], and to the authors' knowledge no data set covers the microstructure, strength, abrasive wear and machinability of sand-cast AA2014/SiC together. Sand casting is attractive for low-volume and large parts, but its slow cooling favors particle pushing and clustering [20], so the useful SiC range cannot simply be taken from faster-cooling routes. The objectives of this study are to (i) characterize the microstructure and phase constitution of AA2014 composites containing 3, 5 and 7 wt.% SiC; (ii) quantify their hardness, tensile strength, abrasive wear and cutting forces; and (iii) relate these properties to the particle distribution and to the strengthening and wear mechanisms, so as to identify the SiC content that gives the best balance of strength, wear resistance and machinability.

Materials and Methods

Materials

AA2014 aluminum alloy was selected as the matrix material because of its high strength and wide use in the aviation and defense industries; its chemical composition is given in Table 1. Commercially available SiC powder (Nanografi Nano Technology, Türkiye; 99%, metals basis) with a particle size of 325 mesh (≤ 44 μm) was used as the reinforcement. The matrix material, equipment and processing route were identical to those used in our earlier study [6], and the values for unreinforced AA2014 are those reported there [6]. For the strengthening and wear calculations, nominal SiC volume fractions of 2.63, 4.39 and 6.16 vol.% and theoretical composite densities of 2.811, 2.818 and 2.825 g/cm³ were obtained from the rule of mixtures, using 2.80 and 3.21 g/cm³ for AA2014 and SiC [36].

Table 1
Chemical composition of the AA2014 matrix alloy (wt.%)

Cr	Cu	Fe	Mg	Mn	Si	Ti	Zn	Al
0.03	4.06	0.47	0.56	0.57	0.60	0.01	0.10	Balance

Fabrication of the Composites

The composites were produced by vortex-assisted stir casting followed by gravity pouring into sand molds; the setup is shown schematically in Fig. 1a. For each heat, about 500 g of AA2014 was melted in a graphite crucible (top diameter 100 mm, height 90 mm) placed in an electric resistance box furnace (SXL-1200). The furnace temperature was set to 900°C and controlled by the furnace thermocouple and temperature control unit. The set temperature was selected in preliminary trials with this furnace and crucible as one that kept the charge fully liquid and stirrable during the additions and stirring. Melting, Mg addition, powder feeding, stirring and standing were carried out with the crucible in the furnace, so that the melt temperature approached the furnace set point; no thermocouple was immersed in the melt. To improve interfacial wettability and lower the surface tension at the particle–matrix interface, 1 wt.% Mg was added to the molten alloy [14, 16]. In parallel, the SiC powder was preheated at 250°C before addition to remove absorbed moisture and to minimize thermal shock on contact with the melt.

An argon atmosphere was maintained throughout the process to prevent oxidation of the molten aluminum. A mechanical impeller immersed in the melt was rotated at 250 rpm to create a stable vortex, and the preheated SiC particles (250°C) were fed into the vortex at a constant rate of 0.75–1.0 g/s. Mixing was continued for 15 min to obtain a uniform dispersion. The melt was then left to stand for 3 min so that entrapped gases could escape before pouring. The crucible was then removed from the furnace, and the composite melt was poured at approximately 800°C into sand molds that produced cylindrical bars of Ø20 × 200 mm, which solidified in still air (Fig. 1b). The production parameters are summarized in Table 2, and the complete processing and testing route is shown in Fig. 1c.

Table 2
Process parameters of vortex-assisted sand casting

Parameter	Value
Heat size	≈ 500 g AA2014
Furnace set temperature (melting and stirring)	900°C
Pouring temperature	≈ 800°C
SiC preheating temperature	250°C
Mg addition	1 wt.%
Stirring speed	250 rpm
Stirring time	15 min
Holding time before pouring	3 min
Powder feed rate	0.75–1.0 g/s
Protective atmosphere	Argon
Mold / casting size	Sand mold, Ø20 × 200 mm

Specimen Preparation

All specimens were taken from the as-cast cylindrical bars (Ø20 × 200 mm). Tensile specimens were machined from the bars to standard dimensions, with the specimen axis parallel to the bar axis. Metallographic, hardness and abrasive wear specimens were sectioned from the outer (near-surface) region of the bars, and the turning tests were performed on the outer surface of the bars.

Microstructural Characterization

Metallographic specimens were ground progressively with SiC abrasive papers from 200 to 1200 grit and finally polished with diamond suspension. Microstructural contrast was developed with Keller's reagent prepared from 95 ml distilled water, 2.5 ml HNO_3, 1.5 ml HCl and 1.0 ml HF. Optical micrographs were taken at ×400. Uneven illumination in the optical micrographs was corrected by dividing each image by its low-pass-filtered background, and brightness and contrast were adjusted uniformly over each image; no local editing was applied. Scanning electron microscopy (SEM; SUPRA 55, Carl Zeiss, Germany) was performed with the secondary-electron (SE2) detector at 15 kV; brightness and contrast were adjusted uniformly, and scale bars were calculated from the pixel size recorded by the instrument. Phases were identified by X-ray diffraction (XRD; Rigaku SmartLab) with Cu Kα radiation (λ = 1.5405 Å) over 2θ = 10–70° at a scan rate of 2°/min and a step of 0.02°. The patterns are presented as recorded, without

smoothing or background subtraction. A reference pattern of Al_4C_3 was calculated from its crystal structure [37].

Mechanical Testing

Vickers hardness was measured with a digital microhardness tester (DHV-1000, Tronic) under a load of 9.81 N (HV1) applied for 15 s. At least five indentations at separate locations were averaged for each material. Cylindrical tensile specimens with a gauge diameter of 6 mm and a gauge length of 30 mm (proportional specimens, $L_o = 5d_o$, EN 10002-1) with threaded heads were machined from the cast bars. They were tested at room temperature on a universal testing machine (Alşa, Türkiye) at a crosshead speed of 1 mm/min.

Abrasive Wear Testing

Two-body abrasive wear was tested at room temperature on a belt-type abrasion tester (Ema EB-125) under a normal load of 25 N. Each specimen slid a total distance of 600 m. The test was stopped every 150 m, and the specimen was cleaned and weighed on an analytical balance with a resolution of 0.1 mg. The interval weight loss was the difference between successive weighings. A new abrasive belt was mounted for each specimen.

Cutting Force Measurement

Turning tests were designed to quantify the influence of SiC content on the cutting forces. All tests were carried out without coolant on a CNC turning center (CS6250B, Baoji Machine Tool Group, China) with uncoated carbide inserts (CCGT 09T301-AS IC20) clamped in an S16Q-SCLCR-09 holder. The spindle speed was 1000 rpm (65 m/min), the depth of cut 0.5 mm and the feed rate 0.05, 0.1 or 0.2 mm/rev (Table 3). The tangential (Fx) and feed (Fy) force components were acquired in real time with a piezoelectric force sensor connected to a charge amplifier and a data logger. All other parameters were kept constant, so that force differences could be attributed solely to the material.

Table 3
Turning conditions

Parameter	Value
Machine	CNC turning center, CS6250B (Baoji Machine Tool Group, China)
Cutting insert	CCGT 09T301-AS IC20, uncoated carbide
Tool holder	S16Q-SCLCR-09
Cutting condition	Dry
Spindle speed	1000 rpm
Cutting speed	65 m/min
Feed rate	0.05, 0.1, 0.2 mm/rev
Depth of cut	0.5 mm

Results and Discussion

Microstructure

Figure 2 shows optical micrographs of the three composites at ×400. In all cases, the etched structure consists of α-Al dendrite cells outlined by a dark interdendritic network, as expected from the slow cooling of sand-cast bars. Dark features are concentrated along this network rather than inside the cells. At 3 wt.% SiC, they occur mainly as small groups along the cell boundaries, with occasional larger dark regions (Fig. 2a, d). At 5 wt.%, the boundary network is decorated more densely, and small rounded pores are also visible (Fig. 2b, e). At 7 wt.%, large dark agglomerates, several times larger than the cells, and rounded pores appear next to particle-poor areas (Fig. 2c, f).

Optical contrast alone cannot distinguish SiC clusters, particle pull-out sites, pores and the interdendritic eutectic, and EDS analysis was not available. The dark features are therefore described as particle-rich regions and associated defects; they are not identified individually as SiC.

The segregation of SiC to interdendritic regions is typical of cast AMCs. During casting, particles are commonly pushed by the advancing α-Al dendrites and trapped in the last liquid to freeze, as observed for TiB_2 particles in as-cast Al–4.5Cu [20]. The low cooling rate of sand molds favors this pushing, so the final particle arrangement follows the dendritic structure rather than the stirring alone. Clustering at 7 wt.% is consistent with the higher apparent viscosity of the melt at larger particle fractions. A more viscous melt weakens the vortex at a fixed speed of 250 rpm, which promotes agglomeration and gas entrapment [1, 13, 14]. Stirring conditions likewise controlled the transition from uniform dispersion to clustering and porosity in SiCp/A356 and ADC12/SiC composites [17, 18].

Secondary-electron SEM micrographs (Fig. 3) show the same arrangement at higher resolution. At 3 wt.% SiC (Fig. 3a, d), a thin interdendritic network with small, isolated bright particles is seen. At 5 wt.% (Fig. 3b, e), the network is denser and locally enriched in particles. At 7 wt.% (Fig. 3c, f), large, bright, angular clusters and particle-rich zones dominate. In secondary-electron images, both SiC particles and the Cu-rich interdendritic eutectic can appear bright, and without EDS the two cannot be separated with certainty. The size and angular shape of the clustered particles are, however, consistent with the ≤ 44 µm SiC powder. No continuous reaction layer could be resolved at these magnifications; EDS mapping or TEM would be needed to characterize the interface.

Figure 4 shows the XRD patterns as recorded, on a square-root intensity scale. All patterns are dominated by the (111), (200) and (220) reflections of α-Al at 2θ ≈ 38.1°, 44.4° and 64.7°, which lie 0.3–0.4° below the reference positions, a uniform shift attributable to specimen displacement. The differences in the relative intensities of the Al peaks reflect the coarse, textured grains of the sand castings. SiC reflections are clearly resolved at 7 wt.% (≈ 34.3°, 35.4° and 59.8°, matching the strongest lines of α-SiC), whereas at 3 and 5 wt.% they are close to the detection limit, as expected for 2.6–4.4 vol.% of a weakly scattering phase in a coarse-grained matrix. The pattern of the 5 wt.% composite has a lower overall intensity and contains a reflection at 29.2° and a broad hump at 13–14° that cannot be assigned to Al, SiC, Al_4C_3 or Si.

Because the melt was held at about 900°C during stirring and standing, the possible formation of Al_4C_3 by $4Al + 3SiC \rightarrow Al_4C_3 + 3Si$ was examined in detail. In the Al–Si–C system, Al_4C_3 coexists with SiC and liquid aluminum above 923 K unless the liquid contains more Si than an equilibrium value that rises with temperature [38]. With only 0.6 wt.% Si, AA2014 offers no such protection, so the reaction is thermodynamically possible at the processing temperature [16, 38]. The calculated Al_4C_3 pattern (Fig. 4, lower panel) shows that its strongest reflections at 40.1°, 55.0°, 31.7° and 35.9° should appear together. No intensity distinguishable from the background was found at 31.7°, 35.9° or 55.0° in any composite. Free Si, which the reaction would also release, was not detected either (28.4°, 47.3° and 56.1°). The weak peak at 39.9° coincides within 0.05° with the Cu Kβ reflection of the Al(200) planes and is therefore not evidence of Al_4C_3. By comparison with the SiC reflections, Al_4C_3 contents above roughly 1 vol.% would have been detected. XRD cannot, however, reveal a thin interfacial reaction layer, and the interface was not examined by EDS or TEM; interfacial carbide formation at the particle surfaces therefore cannot be excluded (see Limitations of the Present Study).

Hardness

Hardness increased monotonically with SiC content, from 33 HV for unreinforced AA2014 to 53, 56 and 64 HV at 3, 5 and 7 wt.% SiC (Fig. 5a). These values represent increases of 61%, 70% and 94%. Under the 9.81 N load, the indentation diagonals were 170–240 µm, much larger than the particles. The measured values therefore reflect the composite response rather than that of individual phases.

Three mechanisms are likely to contribute to the increase. First, the hard particles carry part of the load and constrain plastic flow of the matrix beneath the indenter [39, 40]. Second, the CTE mismatch

between aluminum (≈ 23.6 × 10^{-6} K^{-1}) and SiC (≈ 4–5 × 10^{-6} K^{-1}) generates geometrically necessary dislocations around the particles during cooling, which harden the surrounding matrix [40, 41]. Orowan strengthening is negligible for micrometer-sized particles at these volume fractions [40]. Third, particles restrict dendrite growth and can refine the cast structure [12, 29]. Hardness kept rising between 4.39 and 6.16 vol.%, even where clustering began. Unlike tensile strength, hardness is a local, compressive measure and is not controlled by the weakest flaw. Similar hardness gains were reported for SiC-reinforced 2024 and 2014 alloys produced by stir-based routes [8–10, 12].

Tensile Strength

UTS rose from 92 MPa for the unreinforced alloy to 130 MPa (+ 41%) at 3 wt.% SiC and to a maximum of 143 MPa (+ 55%) at 5 wt.% (Fig. 5b). It then fell to 121 MPa at 7 wt.%. The size of the increase cannot be explained by load transfer alone. The modified shear-lag model for equiaxed particles [39] gives the composite strength σc as

$$\sigma_c = \sigma_m(1 + 0.5V_p)$$

1

where σm is the matrix strength and Vp is the particle volume fraction. With σm = 92 MPa and Vp = 0.026–0.062, Eq. (1) predicts only 93–95 MPa. The measured gain of 38–51 MPa is therefore attributed mainly to the matrix. Likely contributions are dislocation strengthening due to the CTE mismatch and refinement of the as-cast structure [12, 29, 41]. This agrees with strengthening models in which the thermal-mismatch contribution far exceeds that of load transfer [40]. The Mg added as a wetting agent may also contribute, as Mg additions raise the strength of stir-cast SiC-reinforced aluminum alloys [9, 42].

The fall in strength at 7 wt.% is consistent with the clusters and pores seen in Figs. 2 and 3. Clusters act as stress concentrators, and the poorly bonded particles inside them crack or debond at low stress. Cracks then start early and link up through the particle-rich bands, so agglomeration lowers strength and ductility [14, 23, 26]. Porosity also tends to increase with reinforcement content in stir-cast composites [1, 13, 43]. A peak at 5 wt.% followed by a decline at 7 wt.% was reported for AA2014–SiC nanocomposites made by stir-ultrasonic-squeeze casting [10]. The threshold may therefore be a general feature of particle incorporation by stirring rather than of sand casting alone.

Abrasive Wear Behavior

The interval weight loss decreased with sliding distance for all composites, and the 7 wt.% SiC composite lost the least material in every interval (Fig. 6a). After 600 m, the cumulative weight loss was 1.97, 1.82 and 1.49 g for 3, 5 and 7 wt.% SiC (Fig. 6b, Table 4). Raising the SiC content from 3 to 7 wt.% thus reduced the total loss by 24%. In two-body abrasion, hard particles protrude from the worn surface, carry part of the normal load and blunt or deflect the abrasive grits. This reduces furrowing and micro-cutting of the softer matrix [27, 44].

Archard's relation links the wear volume V to the normal load F, the sliding distance L and the hardness H through a dimensionless wear coefficient K [44]:

$$V = K\frac{FL}{H}$$

2

Table 4 lists K calculated from the cumulative volume loss, using the mass loss, the theoretical density and the measured hardness. K varies only from 0.024 to 0.022, so the wear resistance of the composites scales mainly with their hardness. Values of K of the order of 10^{-2} are typical of two-body abrasion [44], which supports micro-cutting by the abrasive grits as the dominant mechanism. The slightly lower K at 7 wt.% suggests an extra protective effect of the particle-rich surface beyond that captured by bulk hardness.

Table 4
Abrasive wear results (25 N, 600 m)

SiC (wt.%)	0–150 m (g)	150–300 m (g)	300–450 m (g)	450–600 m (g)	Cumulative loss (g)	Volume loss (mm^3)	Wear coefficient K
3	0.66	0.51	0.42	0.38	1.97	701	0.024
5	0.61	0.49	0.39	0.33	1.82	646	0.024
7	0.57	0.41	0.29	0.22	1.49	527	0.022

The interval loss fell by 42–61% between the first and last interval. This decline results from progressive degradation of the abrasive belt by grit blunting and clogging with debris, together with smoothing of the initial surface [44]. It was strongest at 7 wt.% SiC (61%), suggesting that protruding SiC particles accelerate grit blunting. Lower wear after SiC addition has also been reported for other cast Al/SiC composites [5, 11, 21, 28, 29, 45]. A reversal at high SiC contents, caused by clustering and particle pull-out, has been observed elsewhere [12], but it did not occur up to 7 wt.% in the present composites. Worn-surface SEM was not available, so the proposed mechanisms rest on the mass-loss data and the hardness correlation.

Cutting Forces

Both force components increased with SiC content and with feed rate (Fig. 7, Table 5). At a feed of 0.05 mm/rev, Fx rose from 29.8 N at 3 wt.% SiC to 34.3 N at 5 wt.% and 36.9 N at 7 wt.%, while Fy rose from 19.4 to 21.4 and 23.1 N. Across the three feeds, raising the SiC content from 3 to 7 wt.% increased Fx by 21–24% and Fy by 15–24%. Quadrupling the feed from 0.05 to 0.2 mm/rev increased Fx by only 5–10% and Fy by 6–11%. The ratio Fy/Fx stayed between 0.61 and 0.65 in all conditions.

Table 5
Cutting forces in dry turning (1000 rpm, ≈ 65 m/min, depth of cut 0.5 mm)

SiC (wt.%)	Feed rate (mm/rev)	Fx (N)	Fy (N)
3	0.05	29.8	19.4
3	0.1	31.4	20.4
3	0.2	32.7	20.7
5	0.05	34.3	21.4
5	0.1	35.6	22.3
5	0.2	35.9	22.7
7	0.05	36.9	23.1
7	0.1	38.6	23.5
7	0.2	39.7	25.7

In particle-reinforced aluminum, the tool must shear the matrix and also fracture, debond or push aside the hard particles in its path [31, 34]. A higher particle fraction increases the number of particles met per unit length of cut and strengthens the matrix, so both force components rise; reinforcement content is accordingly among the most influential machining factors [31, 32]. The weak dependence on feed suggests that ploughing and particle fracture, which depend little on the uncut chip thickness, make up a large part of the force at the small depth of cut and low feeds used here. The general rise of cutting force with feed agrees with results for SiCp/Al composites, in which the force increased with feed and depth of cut [46]. Higher forces also signal faster abrasive wear of uncoated carbide tools, a recognized limitation in machining SiC-reinforced aluminum [31, 33]. The 5 wt.% composite required 5–12% lower forces than the 7 wt.% composite while offering higher strength.

Summary of Structure–Property Relationships

Figure 8 summarizes, schematically, the mechanisms proposed above. At 3 and 5 wt.% SiC, the particles are pushed into the interdendritic regions but remain largely dispersed (Fig. 8a). They carry part of the load and generate CTE-mismatch dislocations in the surrounding matrix without introducing large flaws (Fig. 8c). At 7 wt.%, the larger particle fraction raises the apparent viscosity of the melt, and the particles agglomerate into clusters with associated pores along the interdendritic network (Fig. 8b). These clusters still raise hardness and abrasion resistance but act as crack initiation sites in tension. This would explain why the optimum SiC content differs for strength (5 wt.%) and for wear resistance (7 wt.%).

From a practical standpoint, the three compositions serve different purposes. The 5 wt.% composite gives the highest strength and an 8% lower abrasive loss than the 3 wt.% composite, while requiring 5–

12% lower cutting forces than the 7 wt.% composite. The 7 wt.% composite gives the lowest wear but at the cost of strength and higher tool loading, so it is better suited to parts loaded mainly in sliding or abrasion. Because all properties were measured on the same castings, these trade-offs reflect the effect of SiC content alone rather than differences between processing routes.

Limitations of the Present Study

Several limitations should be noted. First, the melt was processed at a furnace temperature of 900°C, and the pouring temperature (≈ 800°C) was not measured in the melt. These temperatures are higher than recommended for SiC in low-Si aluminum alloys; processing at about 750°C or below, with shorter holding times, would reduce the risk of interfacial reaction and particle settling [16, 38]. Second, although XRD showed no Al_4C_3 or free Si, the particle–matrix interface was not examined by EDS or TEM, so a thin reaction layer cannot be excluded, and the dark features in the optical micrographs could not be identified chemically. Third, porosity and density were not measured, and the reinforcement volume fractions are nominal values. Fourth, all metallographic, hardness and wear specimens were taken from the near-surface region of the cast bars, which solidifies faster than the bar center; through-thickness variations were not evaluated. Finally, fracture and worn surfaces were not examined, so the proposed failure and wear mechanisms rest on the property data.

Conclusions

AA2014 composites containing 3, 5 and 7 wt.% SiC (2.63–6.16 vol.%) were produced by vortex-assisted sand casting. The main conclusions are as follows.

1. Particle-rich regions were located mainly in the interdendritic regions of the coarse sand-cast structure. Distribution was fairly uniform at 3 and 5 wt.%, while clustering and associated porosity became pronounced at 7 wt.%.
2. XRD showed α-Al in all composites and resolved SiC clearly at 7 wt.%. Neither Al_4C_3 nor free Si was detected (detection limit roughly 1 vol.%), although a thin interfacial reaction layer cannot be excluded because the interface was not examined by EDS or TEM.
3. Hardness rose monotonically from 33 HV to 53, 56 and 64 HV (+ 94% at 7 wt.%), which is attributed to load sharing, CTE-mismatch dislocations and structural refinement.
4. UTS peaked at 143 MPa at 5 wt.% SiC (+ 55%) and fell to 121 MPa at 7 wt.% because of clustering and porosity. Load transfer alone accounts for less than 3 MPa of the gain, so matrix-side strengthening dominates.
5. Cumulative abrasive loss after 600 m decreased from 1.97 g to 1.49 g (− 24%) between 3 and 7 wt.% SiC. The nearly constant Archard coefficient (0.022–0.024) indicates that abrasion resistance is governed mainly by hardness.
6. Raising the SiC content from 3 to 7 wt.% increased Fx by 21–24% and Fy by 15–24%, whereas a fourfold increase in feed raised the forces by only 5–11%.
7. The 5 wt.% SiC composite offers the best balance of strength, wear resistance and machinability. The 7 wt.% composite suits wear-dominated parts in which tensile strength is less critical.

Declarations

Conflict of interest

The authors declare that they have no known competing financial interests or personal relationships that could have appeared to influence the work reported in this paper.

Funding

This study was supported by the Mersin University Scientific Research Projects Unit under Project Number 2018-1-TP2-2754.

Author Contribution

Author contributions Berat Baris Buldum: conceptualization, supervision, funding acquisition, resources. Recep Dabak: investigation, data curation, formal analysis. Suleyman Cinar Cagan: methodology, visualization, writing – original draft, writing – review and editing. All authors read and approved the final manuscript.

Acknowledgement

This article is derived from the MSc thesis of Recep Dabak, "Production and physical characterization of ceramic reinforced composite materials with aluminum matrix", Graduate School of Natural and Applied Sciences, Mersin University, 2019.

Data availability

The data supporting the findings of this study are available from the corresponding author on reasonable request.

References

1. S.K. Sharma, S. Gajević, L.K. Sharma, R. Pradhan, Y. Sharma, I. Miletić, B. Stojanović, Progress in aluminum-based composites prepared by stir casting: mechanical and tribological properties for automotive, aerospace, and military applications. Lubricants 12(12), 421 (2024). https://doi.org/10.3390/lubricants12120421
2. S.K. Patel, L. Shi, Recent advances in ceramic-reinforced aluminum metal matrix composites: a review. Alloys 4(3), 18 (2025). https://doi.org/10.3390/alloys4030018

3. C.O. Ujah, D.V. Von Kallon, Trends in aluminium matrix composite development. Crystals 12(10), 1357 (2022). https://doi.org/10.3390/cryst12101357
4. M. Kolev, Metal matrix composites. Encyclopedia 6(7), 139 (2026). https://doi.org/10.3390/encyclopedia6070139
5. A. Chatterjee, S. Sen, S. Paul, P. Roy, A.H. Seikh, I.A. Alnaser, K. Das, G. Sutradhar, M. Ghosh, Fabrication and characterization of SiC-reinforced aluminium matrix composite for brake pad applications. Metals 13(3), 584 (2023). https://doi.org/10.3390/met13030584
6. S.C. Cagan, B.B. Buldum, R. Dabak, Effect of TiC reinforcement on the microstructure and performance of AA2014 composites fabricated via vortex-assisted sand casting. Int. J. Metalcast. (2026). https://doi.org/10.1007/s40962-026-01999-z
7. V. Manokaran, A.X. Michael, Property evaluation of AA2014 reinforced with synthesized novel mixture processed through squeeze casting technique. J. Manuf. Mater. Process. 8(4), 153 (2024). https://doi.org/10.3390/jmmp8040153
8. H.R. Channar, B. Ullah, M.S. Naseem, J. Akhter, A. Mehmood, M. Aamir, Mechanical properties and microstructural investigation of AA2024-T6 reinforced with Al2O3 and SiC metal matrix composites. Eng 5(4), 3023–3032 (2024). https://doi.org/10.3390/eng5040157
9. M. Syahid, H. Arsyad, R. Fibrian, M. Sina, Optimization of stir-squeeze casting parameters of SiC reinforced aluminum composite through Taguchi method. Discov. Appl. Sci. 8 (2026). https://doi.org/10.1007/s42452-026-08651-9
10. P. Verma, J. Ghose, G. Paul, V. Pandey, U. Pandey, Enhanced mechanical and tribological performance of AA2014-SiC metal matrix nanocomposites fabricated by a novel stir-ultrasonic-squeeze casting process. Int. J. Cast Met. Res. 38, 21–35 (2025). https://doi.org/10.1080/13640461.2025.2469026
11. V. Parikh, A. Badgujar, N. Ghetiya, Investigation of microstructural and wear properties of stir cast and friction stir processed AA 2014-based metal matrix composites. Adv. Mater. Process. Technol. 9, 1920–1940 (2023). https://doi.org/10.1080/2374068X.2022.2136688
12. R. Oza, A.B. Dhruv, V. Badheka et al., Ultrasonic-assisted stir casting of SiC-reinforced AA2024 composites: microstructure and mechanical properties. Int. J. Metalcast. (2026). https://doi.org/10.1007/s40962-026-02110-2
13. J. Grilo, V.H. Carneiro, J.C. Teixeira, H. Puga, Manufacturing methodology on casting-based aluminium matrix composites: systematic review. Metals 11(3), 436 (2021). https://doi.org/10.3390/met11030436
14. A. Kareem, J. Abu Qudeiri, A. Abdudeen, T. Ahammed, A. Ziout, A review on AA 6061 metal matrix composites produced by stir casting. Materials 14(1), 175 (2021). https://doi.org/10.3390/ma14010175
15. P.K. Gurmaita, R. Pongen, S.K. Gurmaita, A7075 alloy reinforced metal matrix composites fabricated through stircasting route: a review. Int. J. Cast Met. Res. 37, 208–255 (2024). https://doi.org/10.1080/13640461.2024.2355634

16. M. Malaki, A. Fadaei Tehrani, B. Niroumand, M. Gupta, Wettability in metal matrix composites. Metals 11(7), 1034 (2021). https://doi.org/10.3390/met11071034
17. R. Jiang, R. Hu, R. Li, C. Zhang, A. Fu, L. He, Influence of stirring speed, temperature, and time on SiCp/A356 composite properties via stir-casting. Int. J. Metalcast. (2026). https://doi.org/10.1007/s40962-026-01968-6
18. C. Morsiya, S. Pandya, V. Badheka, K. Mehta, Effect of stirrer blade geometry on particle dispersion and properties of ADC12/SiC composites. Int. J. Metalcast. (2026). https://doi.org/10.1007/s40962-026-01978-4
19. M. Ostad Shabani, A. Baghani, I. Mobasherpour, M. Razavi, M. Rahimipour, E. Salahi, The influence of the casting methods and variables on the microstructural properties of A356–SiC nanocomposite. Int. J. Metalcast. 18, 3420–3434 (2024). https://doi.org/10.1007/s40962-024-01267-y
20. Q. Han, Y. Liu, C. Peng, Z. Liu, Engulfment of a particle by a growing crystal in binary alloys. Crystals 12(10), 1421 (2022). https://doi.org/10.3390/cryst12101421
21. V. Chak, H. Chattopadhyay, Mechanical and tribological properties of ceramic–aluminium composites developed using stirring-assisted squeeze casting. Int. J. Cast Met. Res. 36, 65–75 (2023). https://doi.org/10.1080/13640461.2023.2207894
22. R. Venkatesh, I. Hossain, V. Mohanavel, M. Soudagar, S.A. Alharbi, S. Al Obaid, Enriching performance of Al-Mg composites by incorporating nano-alumina and SiC via semi-solid stir processing. Int. J. Cast Met. Res. 38, 50–60 (2025). https://doi.org/10.1080/13640461.2025.2476826
23. H. Mehdi, S. Bhati, P. Mouria, S. Mishra, M. Bhadana, L. Batra, Effect of nanoparticles on metal matrix composites fabricated by ultrasonic stir casting. Int. J. Cast Met. Res. 38, 157–173 (2025). https://doi.org/10.1080/13640461.2025.2496607
24. R. Singh, R. Kumar, V.P. Singh, Synergistic effect of reinforcement (10 wt.% SiC) in Al-7Si LM25 alloy-based metal matrix composites and heat treatment-driven mechanical and tribological stability. Int. J. Metalcast. (2026). https://doi.org/10.1007/s40962-026-01972-w
25. M. Ekpu, S. Ikpeseni, Characterising the mechanical properties of a composite material comprising aluminium and silicon carbide. Silicon 16, 4333–4342 (2024). https://doi.org/10.1007/s12633-024-03006-8
26. F. Rocha, S. Simões, Production and characterization of aluminum reinforced with SiC nanoparticles. Metals 13(9), 1626 (2023). https://doi.org/10.3390/met13091626
27. Y. Wang, J. Zhang, A review of the friction and wear behavior of particle-reinforced aluminum matrix composites. Lubricants 11(8), 317 (2023). https://doi.org/10.3390/lubricants11080317
28. S. Mustafa, J. Haider, P. Matteis, Q. Murtaza, Synthesis and wear behaviour analysis of SiC- and rice husk ash-based aluminium metal matrix composites. J. Compos. Sci. 7(9), 394 (2023). https://doi.org/10.3390/jcs7090394
29. D. Zhou, X. Liu, M. Yang, Microstructure and wear resistance of (Mg2Si + SiCp)/Al composites. Metals 16(1), 111 (2026). https://doi.org/10.3390/met16010111

30. M. Surya, G. Prasanthi, Effect of SiC weight percentage on tribological characteristics of Al7075/SiC composites. Silicon 14, 1083–1092 (2022). https://doi.org/10.1007/s12633-020-00885-5
31. P. Sarmah, K. Gupta, A review on the machinability enhancement of metal matrix composites by modern machining processes. Micromachines 15(8), 947 (2024). https://doi.org/10.3390/mi15080947
32. M.R.K. Reddy, S. Gugulothu, T. Krishnaiah, A comparative analysis of microstructure and machinability of stir-casted and 3D-printed Al-Cu-SiC-GNP metal matrix composites using ML, TLBO and RAO-II techniques. Adv. Mater. Process. Technol. 11, 3940–3959 (2025). https://doi.org/10.1080/2374068X.2025.2530980
33. E.E. Ashkinazi, S.V. Fedorov, A.K. Martyanov et al., Wear of carbide plates with diamond-like and micro-nano polycrystalline diamond coatings during interrupted cutting of composite alloy Al/SiC. J. Manuf. Mater. Process. 7(6), 224 (2023). https://doi.org/10.3390/jmmp7060224
34. B. Zhao, J.-H. Peng, W.-F. Ding, Machined surface formation and integrity control technology of SiCp/Al composites: a review. Surf. Sci. Technol. 1 (2023). https://doi.org/10.1007/s44251-023-00011-8
35. D. Reddy, K. Manjunath, N. Narendra et al., Hard titanium carbide particles impact on the microstructure, mechanical and wear behavior of Al2014 alloy composites. J. Bio Tribo Corros. 12 (2026). https://doi.org/10.1007/s40735-026-01199-6
36. I.A. Ibrahim, F.A. Mohamed, E.J. Lavernia, Particulate reinforced metal matrix composites — a review. J. Mater. Sci. 26(5), 1137–1156 (1991). https://doi.org/10.1007/BF00544448
37. T.M. Gesing, W. Jeitschko, The crystal structure and chemical properties of U2Al3C4 and structure refinement of Al4C3. Z. Naturforsch. B 50(2), 196–200 (1995). https://doi.org/10.1515/znb-1995-0206
38. J.C. Viala, P. Fortier, J. Bouix, Stable and metastable phase equilibria in the chemical interaction between aluminium and silicon carbide. J. Mater. Sci. 25(3), 1842–1850 (1990). https://doi.org/10.1007/BF01045395
39. V.C. Nardone, K.M. Prewo, On the strength of discontinuous silicon carbide reinforced aluminum composites. Scr. Metall. 20, 43–48 (1986). https://doi.org/10.1016/0036-9748(86)90210-3
40. O. Matvienko, O. Daneyko, T. Kovalevskaya, A. Khrustalyov, I. Zhukov, A. Vorozhtsov, Investigation of stresses induced due to the mismatch of the coefficients of thermal expansion of the matrix and the strengthening particle in aluminum-based composites. Metals 11(2), 279 (2021). https://doi.org/10.3390/met11020279
41. R. Zhang, C. Zou, Z. Wei, H. Wang, Microstructural evolution and mechanical properties of SiC/Al-40Si composites fabricated by high pressure solidification. Materials 16(12), 4312 (2023). https://doi.org/10.3390/ma16124312
42. A. Shetty, S. Sharma, T. Bhat, A. Hegde, G. Anne, R. Prabhu, R. Bhat, Hardness, tensile and microstructural characteristics of stir cast Al–Si eutectic matrix SiC-reinforced composites in as-

cast and peak-aged conditions. Discov. Appl. Sci. 8 (2026). https://doi.org/10.1007/s42452-026-09213-9

43. V. Singhal, D. Shelly, A. Saxena, R. Gupta, V.K. Verma, A. Jain, Study of the influence of nanoparticle reinforcement on the mechanical and tribological performance of aluminum matrix composites—a review. Lubricants 13(2), 93 (2025). https://doi.org/10.3390/lubricants13020093
44. I.M. Hutchings, P. Shipway, Tribology: Friction and Wear of Engineering Materials, 2nd edn. (Butterworth-Heinemann, Oxford, 2017)
45. P. Gupta, P.V.R. Ramana Rao, A study on mechanical and tribological properties of aluminium 6061-SiC-B4C-GO hybrid nanocomposites with a novel optimized mix selection approach. Int. J. Cast Met. Res. 37, 81–107 (2024). https://doi.org/10.1080/13640461.2023.2293406
46. R.A. Laghari, J.-G. Li, Modeling and optimization of cutting forces and effect of turning parameters on SiCp/Al 45% vs SiCp/Al 50% metal matrix composites: a comparative study. SN Appl. Sci. 3 (2021). https://doi.org/10.1007/s42452-021-04689-z

Figures

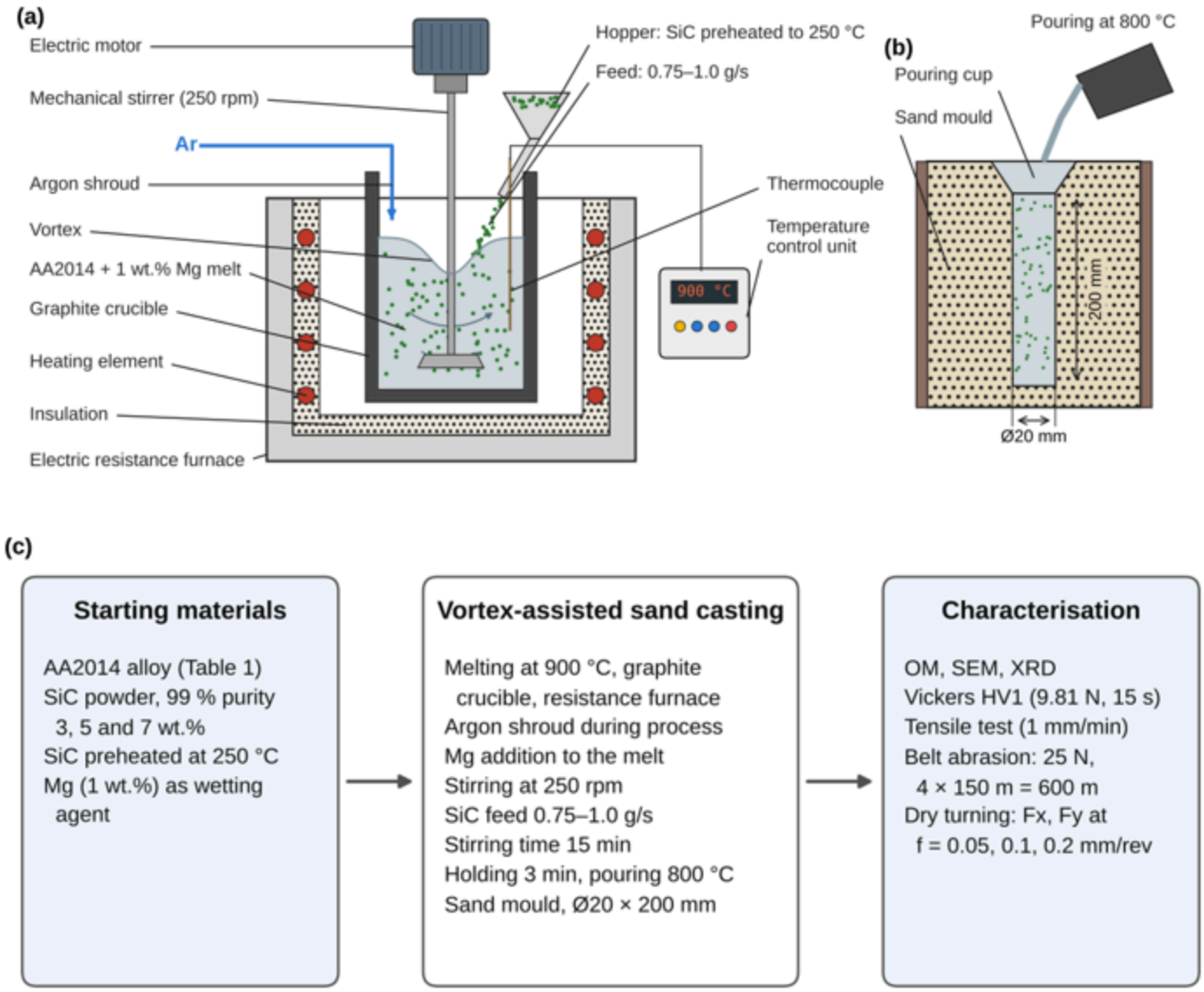


Figure 1

(a) Schematic of the vortex-assisted stir casting setup, (b) pouring of the composite slurry into the sand mould and (c) processing and characterisation route used for the AA2014/SiC composites.

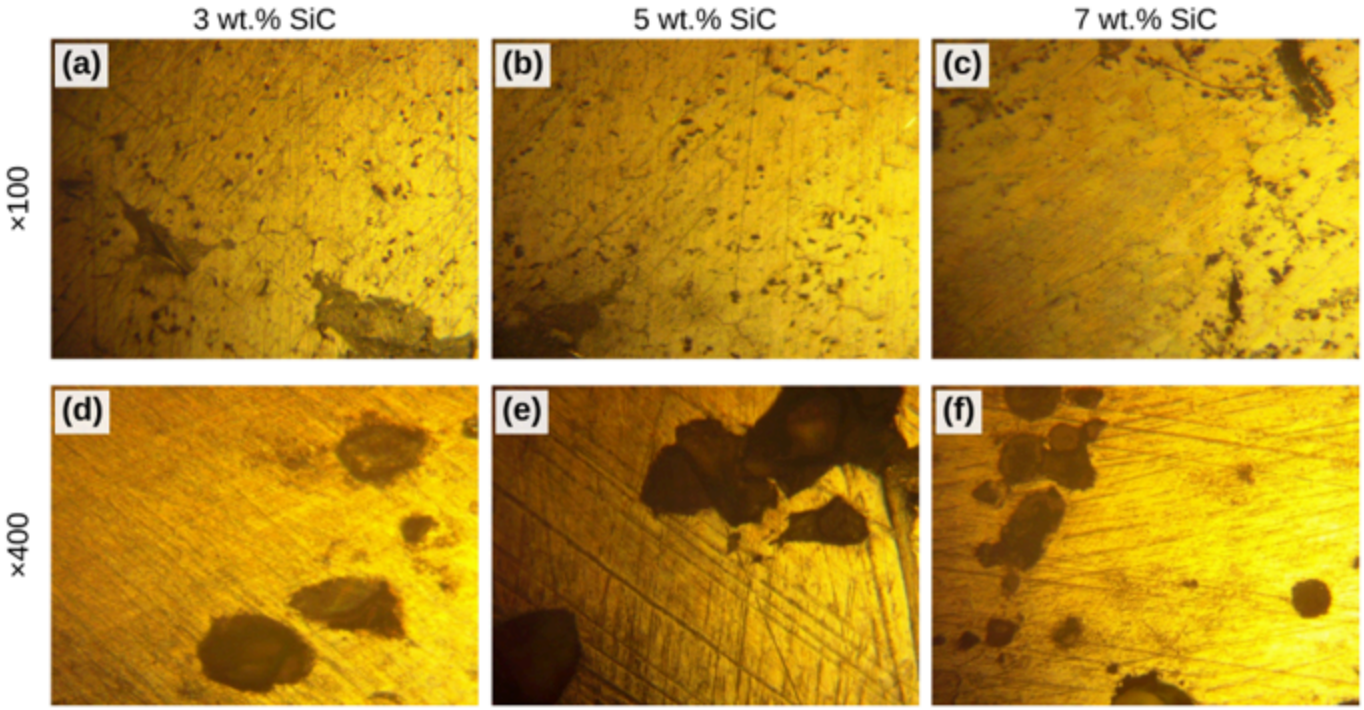


Figure 2

Optical micrographs of AA2014 composites containing (a, d) 3, (b, e) 5 and (c, f) 7 wt.% SiC at ×100 (a–c) and ×400 (d–f).

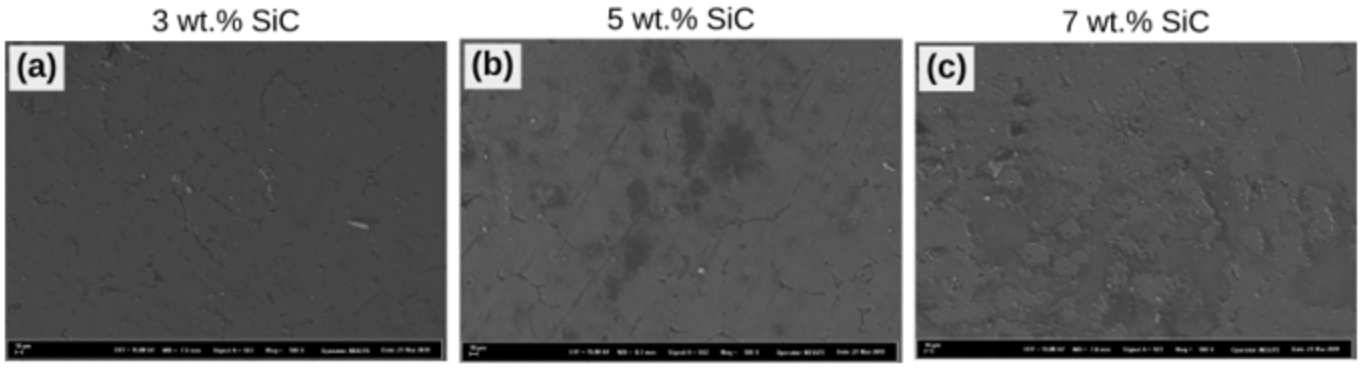


Figure 3

SEM micrographs (secondary electrons, 15 kV, ×500) of AA2014 composites containing (a) 3, (b) 5 and (c) 7 wt.% SiC.

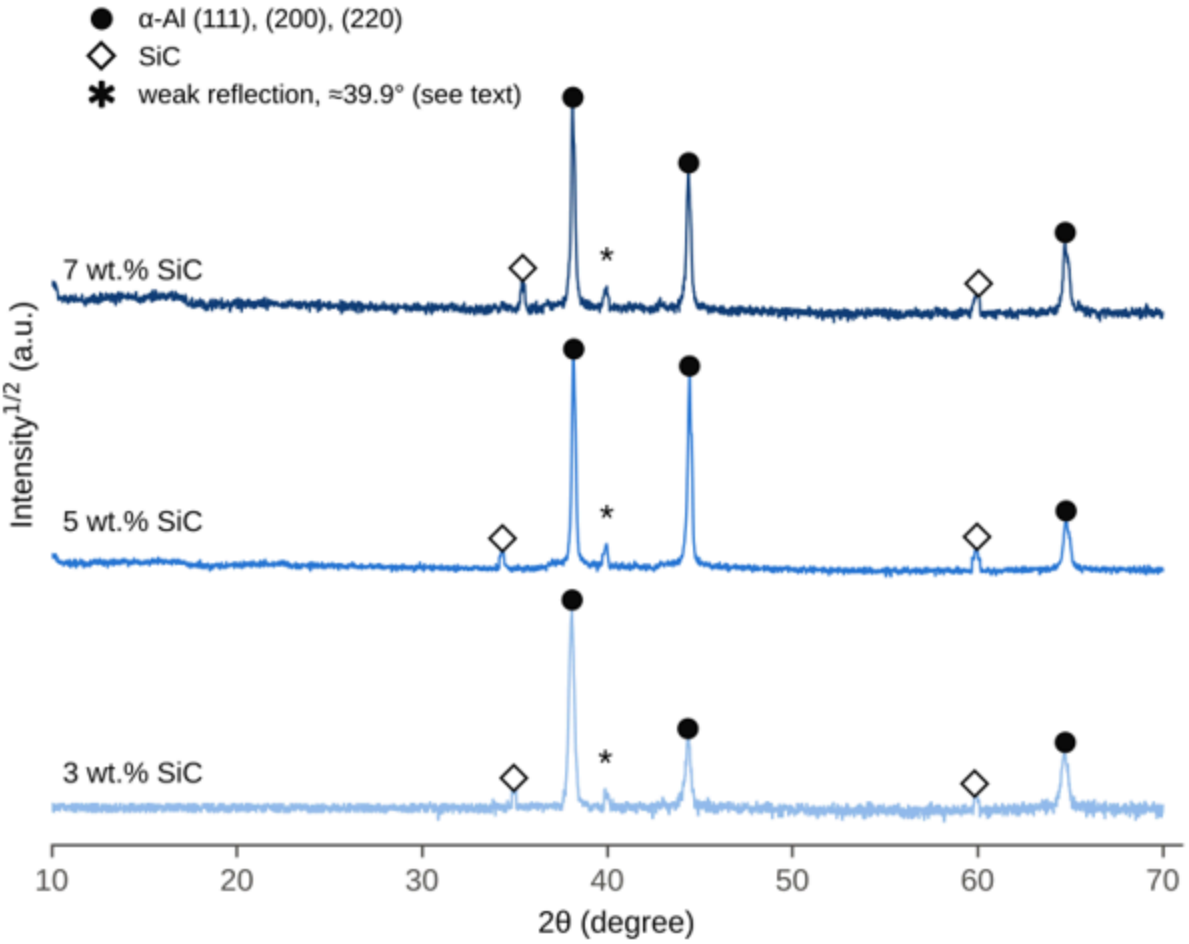


Figure 4

XRD patterns of the AA2014/SiC composites, plotted on a square-root intensity scale.

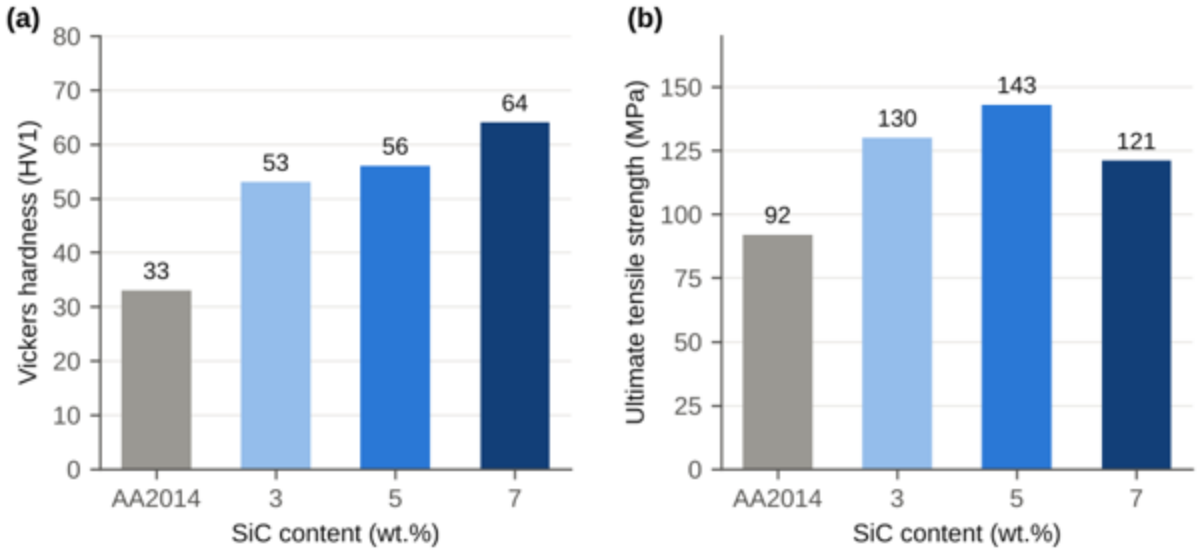


Figure 5

(a) Vickers hardness and (b) ultimate tensile strength of unreinforced AA2014 and the AA2014/SiC composites.

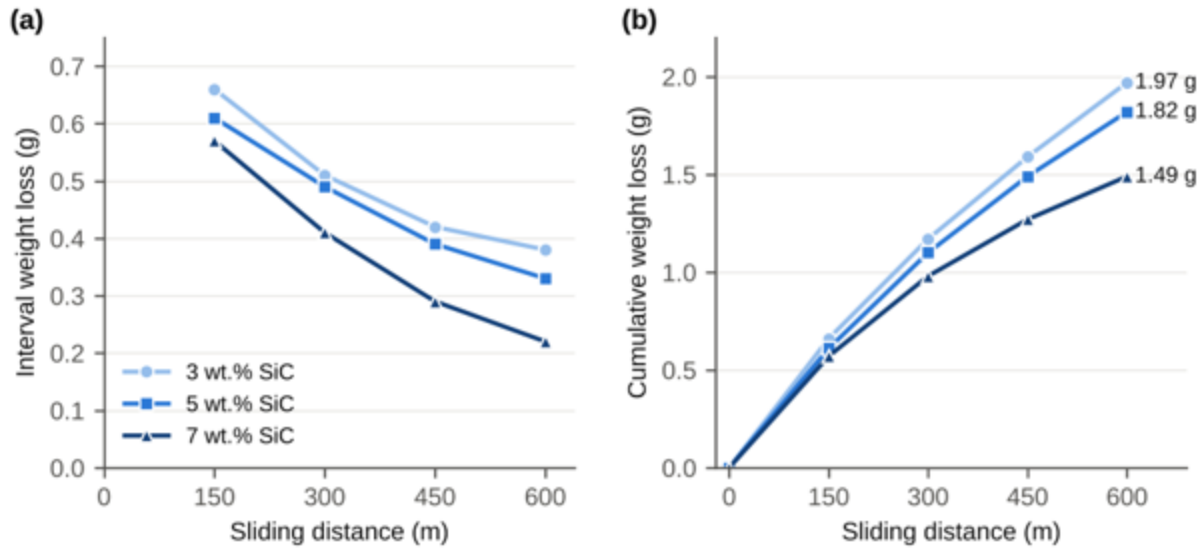


Figure 6

(a) Interval and (b) cumulative weight loss versus sliding distance in belt abrasion under 25 N.

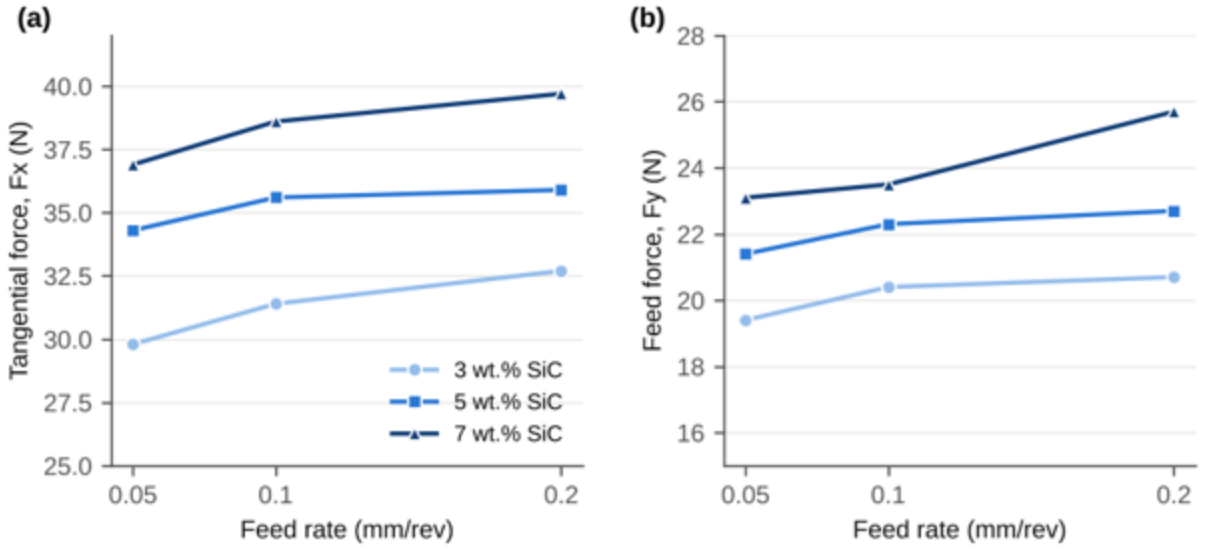


Figure 7

(a) Tangential force Fx and (b) feed force Fy versus feed rate in dry turning (1000 rpm, depth of cut 0.5 mm).

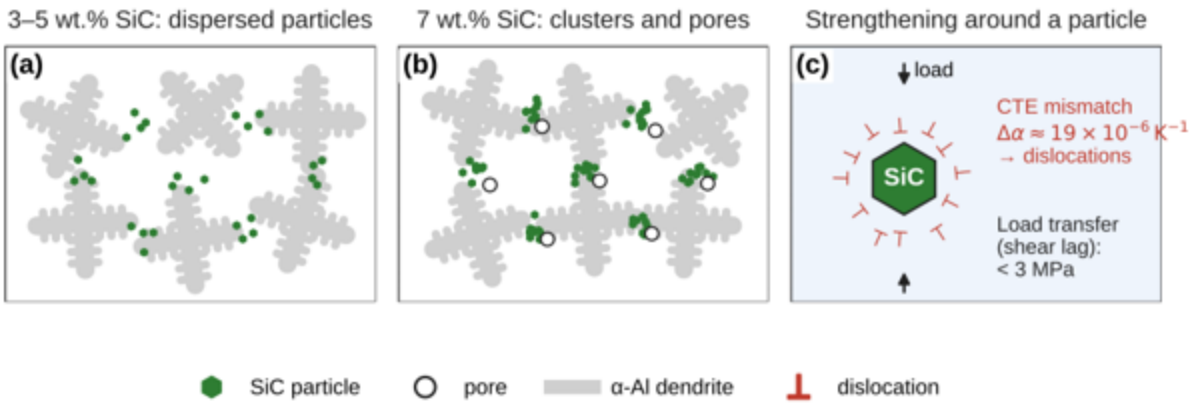


Figure 8

Schematic of the microstructure–property relationships in the sand-cast AA2014/SiC composites: (a) dispersed particles in the interdendritic regions at 3–5 wt.% SiC, (b) particle clusters and pores at 7 wt.% SiC and (c) strengthening by CTE-mismatch dislocations and load transfer around a SiC particle.